1

3

4 **Nanopores in hematite (α-Fe_2O_3) nanocrystals observed by electron tomography**

5

6 Takuya Echigo[†,‡,*,1], Niven Monsegue[§,‖], Deborah M. Aruguete[†,§,2],

7 Mitsuhiro Murayama[§,‖] and Michael F. Hochella Jr.[†,§],

8 [†] Center for NanoBioEarth, Department of Geosciences, Virginia Tech, Blacksburg, VA 24061, USA

9 [‡] Japan International Research Center for Agricultural Sciences,

10 Ohwashi 1-1, Tsukuba 305-8686, Ibaraki, JAPAN

11 [§] Institute for Critical Technology and Applied Science, Virginia Tech, Blacksburg, VA 24061, USA

12 [‖] Department of Materials Science and Engineering, Virginia Tech, Blacksburg, VA 24061, USA

13 [1] Present address: Functional Geomaterials Group, Environmental Remediation Materials Unit,

14 National Institute for Materials Science, 1-1 Namiki, Tsukuba, Ibaraki 305-0044, JAPAN

15 [2] Present address: Division of Earth Sciences, National Science Foundation, 4201 Wilson Boulevard,

16 Arlington, VA 22230, USA

*Corresponding author: Takuya Echigo, email:

18 ECHIGO.Takuya@nims.go.jp

19

ABSTRACT

We report the first characterization of the internal structural features within rhombohedral nanocrystals of hematite (α-Fe_2O_3), specifically nanoscale pores (nanopores) within these crystals observed by HAADF-STEM (high-angle annular dark-field scanning transmission electron microscopy) tomography. Three-dimensional observations of the internal structure of hematite nanocrystals suggest that the nanopores are formed due to a large reduction in solid volume during the transformation of a poorly crystalline precursor (aggregates of ferrihydrite: $Fe_{8.2}O_{8.5}(OH)_{7.4}{\cdot}3H_2O$), which results in the formation of pores between grain boundaries. We also discuss dissolution experiments of the hematite nanocrystals in ascorbic acid solution, in which we demonstrated that the nanopores are reactive sites for dissolution and enlarged by preferential etching.

KEYWORDS Iron oxide nanoparticle, hematite, nanopore, scanning transmission electron microscopy, electron tomography, Kirkendall effect

INTRODUCTION

Iron oxide and iron (oxy)hydroxide minerals, hereafter iron oxides, are present in almost all of the various compartments of the Earth's surface global system — the atmosphere, hydrosphere, crustal lithosphere, pedosphere and biosphere — and take part in the manifold interactions between these compartments. Much of the iron oxide in nature is found as nano-sized particles (nanoparticles)

in, for example, soil (e.g. Waychunas et al. 2005), river water (e.g. Hochella et al. 2005), airborne mineral dust (e.g. Utsunomiya and Ewing 2003), living organisms (e.g. Banfield et al. 2000) and even Martian environments (e.g. Christensen et al. 2001). The pattern of occurrence and distribution of different iron oxides in nature are affected by particle size (Navrotsky et al. 2008; Navrotsky et al. 2010) as well as other extrinsic parameters such as pH, temperature and pressure. The biogeochemical and ecological impacts of nano-sized iron oxides and other nanominerals and mineral nanoparticles are some of the fastest growing areas of research today (Wigginton et al. 2007; Hochella et al. 2008; Echigo et al. 2012).

Hematite, α-Fe_2O_3, is one of most common iron oxides in nature, and exhibits various crystal morphologies, e.g. rhombohedra, hexagonal plates, ellipsoids, and other anhedral forms; and surface topography, e.g. steps, kinks, spirals, and hollow cores (Sunagawa 2005). These variations in crystal morphology and surface topography reflect the varying physical and chemical conditions of the environments during mineral formation and subsequent dissolution (Boudeulle and Muller 1988; Schwertmann et al. 1998; Hochella et al. 1999; Carbone et al. 2005). In addition, hematite nanoparticles have attracted considerable attention from the standpoint of environmental remediation (e.g. Bargar et al. 1999; Redman et al. 2002), photo-chemical catalyst (e.g. Kormann et al. 1989; Eggleston et al. 2009), and magnetic material application (e.g. Kletetschka et al. 2000; Wu et al. 2006). In general, particle size, crystal morphology, and defects are important factors influencing many interactions between solids and liquids, including dissolution, adsorption, electron transfer and

magnetic properties. Thus, understanding coarsening behavior, morphology evolution and defect generation is essential for efficient material design and quality control as well as understanding geologic significance as alluded to above.

In natural environments, hematite typically forms as a result of the weathering of Fe-containing minerals (Cornell and Schwertmann 2003). In this process, nanoparticles of a poorly crystalline iron oxide, ferrihydrite ($Fe_{8.2}O_{8.5}(OH)_{7.4}\cdot 3H_2O$; Michel et al. 2010), forms initially and eventually crystallizes into hematite (Jambor and Dutrizac 1998). Nanoparticles of hematite or other synthetic iron oxides used for pigments and magnetic materials are commonly produced as precipitates from ferrous/ferric salt solution via the same precursor at industrial scale (Buxbaum 1998; Myerson 2002). This suggests that the transformation of ferrihydrite into hematite is critical for the crystal growth of hematite in both industrial and environmental settings. The mechanism and kinetics of the transformation from ferrihydrite into hematite have been studied both theoretically (Tsukimura et al. 2010) and experimentally by TEM (Fischer and Schwertmann 1975), X-ray and neutron scattering (Christensen et al. 1980), Mössbauer spectroscopy (Johnston and Lewis 1983; Schwertmann and Murad 1983), oxygen isotope fractionation experiments (Bao and Koch 1999) and synchrotron-based in-situ XRD (Vu et al. 2008). It is concluded, from nearly all of these studies, that the nucleation and growth of nano-sized hematite involves a combination of aggregation, dehydration and condensation reactions among the particles of ferrihydrite (Cornell et al. 1989). Note that transformation of ferrihydrite into hematite in Cl-containing solution occurs through an intermediate phase, akaganeite

77 [FeO(OH, Cl)], which was also investigated using TEM (Shindo et al. 1993, Park et al. 1996,
78 Sugimoto et al. 1998, Peng et al. 2010). While it might be postulated that evidence of these
79 formation mechanisms would be present within nanohematite, the internal structure has not
80 previously been directly characterized, due to the small particle size. We therefore performed
81 microscopic observations of the internal structure of nanocrystalline hematite in order to gain insight
82 concerning its coarsening behavior and morphological evolution, as well as the origin of crystal
83 defects.

84 In this study, we provide the first report concerning the internal structure of rhombohedral
85 hematite nanocrystals imaged by HAADF-STEM (high-angle annular dark-field scanning
86 transmission electron microscope) tomography which provides three-dimensional information on the
87 nanoscale structure of nanomaterials (Rösner et al. 2007; Fujita et al. 2008; Klein et al. 2011). Our
88 results demonstrate the existence of nanoscale pores (nanopores) within the nanocrystals.
89 Furthermore, we perform dissolution experiments of the hematite nanocrystals using ascorbic acid as
90 a reductant and find that these nanopores act as reactive sites for reductive dissolution which is the
91 most important dissolution mechanism of iron oxide in the natural environment (Cornell and
92 Schwertmann 2003). These experimental observations afford important insights into the formation
93 mechanism of nano-sized single crystals of hematite and how certain reactive sites on the surface of
94 these nanocrystal form during crystal growth.
95

EXPERIMENTAL METHODS

Hematite nanoparticles examined in this study were synthesized by forced hydrolysis of an acidic ferric nitrate solution (Fischer and Schwertmann 1975; Matijević and Scheiner 1978). 500 mL of 0.002 M HCl within a screw-cap HDPE bottle were heated to 98 °C in an oven. The solution was then quickly removed from the oven, and 4.04 g of $Fe(NO_3)_3 \bullet 9H_2O$ were added. Immediately, the mixture was vigorously agitated in the bottle. The bottle was returned to the oven and held at 98 °C for 7 days. After this aging, the suspension was cooled overnight and dialyzed 10 times with 6000-8000 molecular-weight-cutoff tubing against 3,000 mL of MilliQ doubly distilled water, a process that generally took four days. The dialyzed suspension was poured from the tubing into HDPE bottles and stored at 4 °C.

Powder X-ray diffraction was performed to identify mineral phases in the synthesized product using a PANnalytical X'Pert PRO diffractometer equipped with a Cu source and an X-Celerator detector. Data points were collected over the range 8-80° 2θ at a scan rate of 0.6°/min. The diffraction pattern was compared to reference powder diffraction files (PDFs) for hematite (#33-664), which revealed that the product was hematite and had no other detectable crystalline phases. The shape and average size of the synthesized particles were examined with a Philips EM420 transmission electron microscope (TEM) operated in bright field mode at 120 kV. Each TEM sample was prepared by diluting one drop of hematite suspension into 5 mL of MilliQ water. This mixture was then sonicated for ten minutes. A drop of the resulting diluted suspension was deposited onto a 3

115 mm 400 mesh carbon coated copper grid (Electron Microscopy Science Inc.) and allowed to air-dry.
116 High-resolution TEM images of hematite nanocrystals were collected in order to observe nanoscale
117 structures, *e.g.*, surface roughness, lattice fringes, and defects with FEI TITAN 300 operated at
118 200kV.

119 Electron tomography was performed also with the FEI Titan 80-300 TEM operated at 200 kV
120 and double film (ultra thin continuous carbon film reinforced by lacey carbon layer) coated copper
121 grids (Cu-200HD, Pacific Grid-Tech). Tilt-series were acquired in High Angle Annular Dark Field
122 (HAADF) - Scanning Transmission Electron Microscope (STEM) mode using a Fischione Model
123 3000 Annular Dark Field detector at a beam convergence (half-angle) of 10.5 mrad and a Fischione
124 2020 ultrahigh-tilt single-axis tomography holder. Images were recorded every 1° in the tilt range of
125 -65 to +65°. Hardware calibrations and software parameters were refined to improve tilt series
126 acquisitions at high magnification. These parameters included: defocus, image shift, and specimen
127 holder tilt shift. Following an acquisition of a tilt series, images were spatially aligned by
128 cross-correlation algorithm using FEI Inspect 3D Express software. A Simultaneous Iterative
129 Reconstruction Technique (SIRT) was used to reconstruct data sets and 3D Visualization was
130 performed using FEI Resolve RT.

131 In this study, we also conducted dissolution experiments to examine the morphological
132 evolution of hematite nanocrystals. These experiments were conducted with hematite nanoparticles
133 on a 3 mm 400 mesh carbon-coated gold grid (Electron Microscopy Science Inc.) prepared as

mentioned above. Ascorbic acid was used as a reducing agent. The experiments were performed in a catalytically maintained anaerobic environment (vinyl anaerobic chamber of Coy Laboratory Products Inc., ~1% H_2 and O_2 < 100 ppm, as measured by an oxygen/hydrogen gas analyser). The solution conditions for the dissolution experiments were as follows: 5.0 mM ascorbate as the reductant, and 10 mM sodium nitrate as the background electrolyte in 80 mM acetate buffer (pH = 3.35). The total volume was 200 mL. We purged the ascorbate solution with nitrogen for 10 minutes, and then immediately transferred the solution to the anaerobic chamber. The ascorbate solution was transferred to a 250 mL Teflon beaker and magnetically stirred for at least 2 hours to equilibrate the reaction temperature. The hematite nanocrystal sample (TEM grid coated with nanocrystals, prepared as mentioned above) was secured to a Nalgene HDPE TEM grid holder. To initiate the dissolution reaction, this assembly was immersed in the ascorbate solution. The beaker was covered with aluminum foil to prevent light exposure, and the solution was maintained under constant magnetic stirring at 23.0 ± 0.5 °C. Temperature was monitored throughout the experiment period (5 hours). After the reaction, the TEM grid was removed from the ascorbate solution, washed with Milli-Q water and dried in the anaerobic chamber.

RESULTS AND DISCUSSION

Observation of nanoporous structure within the hematite nanocrystals

Hematite nanoparticles were synthesized for this study by forced hydrolysis of ferric nitrate

and aging, resulting in monodisperse rhombohedral crystals with an average size of 30.5 nm (Fig. 1). Rhombohedral nanohematite prepared in a similar fashion was investigated using HRTEM and AFM (Rodriguez et al. 2007). The authors concluded that the crystal faces truncating the particle surfaces were consistent with the {104} family of crystal planes. This rhombohedral shape is the principal habit for synthetic hematite (Cornell and Schwertmann 2003).

A high-resolution TEM (HRTEM) image of the hematite nanocrystals is shown in Figure 2a. In this image, a bright area (approximately 5 nm in diameter) can be observed near the middle of a crystal face. This HRTEM image shows regular lattice fringes right up to the edge of this area, suggesting that the crystal structure of this hematite nanoparticle is durable under electron irradiation and therefore this area is not a consequence of electron beam damage. It is well known that contrast in TEM images is generated by several factors, *e.g.*, scattering, diffraction, and phase contrast (Reimer and Kohl 2008), and thus simulation of HRTEM images using, for example, the multi-slice method (Cowley and Moodie 1957), allows us to investigate the structure of defects and distribution of vacancies within the examined material (Cook et al. 1983, Janney and Banfield 1998, Kogure and Inoue 2005). However, simulation methods are generally best applied in cases where the atomic arrangement (or coordinates) of the defect is known, or energetically predicted via computation. Otherwise, results from simulation could be inconclusive. It should be noted that there is no universal theory capable of predicting atomic arrangements in metastable or defective crystals. While the bright area in Figure 2a is diamond-shaped, it does not appear to be a crystallographically

oriented structure relative to the matrix that shows {104} faces. Hence it is not practical to simulate this HRTEM image (Fig. 2a) to infer whether this 5 nm diamond-shaped region is a cavity or a localized disordered structure such as an amorphous phase or a highly strained area. In addition, a TEM image is a two-dimensional projection of a sample along the electron optic axis. The resulting image loses spatial resolution in the depth (sample thickness) direction, and therefore it is not sufficient to determine three-dimensional geometrical relationships. Such three-dimensional information on the nanoscale physical structure of a nanomaterial can be obtained using electron tomography (Rösner et al. 2007; Fujita et al. 2008; Klein et al. 2011). Among various methods for imaging, e.g., bright-field TEM (BF-TEM) and annular-dark-field STEM (ADF-STEM), HAADF-STEM is most suitable for tomography of nanometer-sized crystals because of its higher signal-to-noise ratio and smaller effect of electron diffraction on the image contrast than other techniques (Friedrich et al., 2005). Hence we employed the HAADF-STEM tomography technique to examine both the external and internal form of hematite nanoparticles in three dimensions, as discussed below.

A HAADF-STEM image of a small aggregate of hematite nanocrystals is shown in Figure 2b. In this image, the circular region shows dark contrast. Since the contrast in the HAADF-STEM image is mainly attributed to the atomic number of the target material, the darker contrast in a single phase hematite particle suggests that the circular region is much lower in density, making it most likely that the cavity is a hollow-type defect structure. An isosurface image calculated from a

191 reconstructed HAADF-STEM tomography tilt series of this small aggregate is shown in Figure 2c
192 (see Movie 1 in the Data Repository available online). This three-dimensional reconstruction
193 demonstrates that this hematite has a nanoscale pore that appears on the surface of one of the crystals.
194 In addition, a slice of the reconstructed image of the hematite (Fig. 2d) reveals that this hematite is
195 nanoporous, with nanoscale pores occurring within the crystals. However, it is well known that the
196 electron beam can cause crystal damage of oxide nanoparticles such as amorphitization and
197 decomposition (Storm et al. 2005; Shi et al. 2007). In the following section, we consider whether
198 these observed nanoporous internal structures are generated by electron beam damage.

199 In both Figures 3a and 3b, nanopores in multiple hematite nanocrystals are clearly visible.
200 Figures 3a and 3b were taken in STEM and TEM mode, respectively, using a field emission source at
201 200 kV. The electron dose in STEM mode is a couple of orders of magnitude higher than TEM mode,
202 yet they both show the same types of nanopores. As mentioned above, the same structures are also
203 observed in Figure 1 which was imaged at much lower magnification using a thermo-emission
204 source (tungsten filament) at 120 kV. Together, all of these (S)TEM images suggest that the
205 nanopores are not generated by electron beam damage because the electron dose of a
206 thermo-emission source is dramatically lower than that of a field emission source. In addition, the
207 TEM images that were taken immediately after inserting the sample and after about 15 minutes of
208 exposure are shown in Figures 4a and 4b, respectively. These images afford experimental evidence
209 that nanopores in the hematite nanocrystal were not formed by electron beam damage and they do

not develop with increased electron dose. These images also show one nanocrystal of hematite that has irregular morphology, which supports the interpretation that aggregation of precursor nanoparticles (ferrihydrite) precedes the crystallization of nano-hematite as discussed below.

Nanopores as reactive sites of hematite nanocrystals

We have conducted dissolution experiments with ascorbic acid to examine morphological changes of hematite during the dissolution process; typical examples of HRTEM images of hematite before and after dissolution are shown in Figures 5a and 5b, respectively. The dramatic enlargement of the funnel-shaped openings of pre-existing nanopores that reach the surface was observed after dissolution, which strongly suggests that these openings provide highly reactive sites for dissolution. Ascorbic acid is a strong reductant and its dissolution activity involves the reduction of iron from ferric to ferrous (Banwart et al. 1989; Dos Santos Afonso et al. 1990; Suter et al. 1991; Echigo et al., 2012). It is impossible to elucidate whether or not the electron transfer preferentially occurs around these nanopores because electron transfer reactions at one surface of hematite can couple with iron reduction at another site *via* current flow through the crystal bulk due to the semi-conducting nature of hematite (Yanina and Rosso 2008). However our observations still demonstrate that the nanopores are reactive sites for dissolution.

Formation mechanism of the nanoporous structure

Nanoscale pores (also known as "nanopipes"), somewhat similar to what is seen here in nanohematite, are commonly observed in SiC (Si et al. 1997), GaN (Jacobs et al. 2008), canavalin (Land et al. 1995) and lysozime (Heijna et al. 2006) crystals and their formation mechanism is explained in terms of the spiral growth from screw dislocation. The formation of nanoscale hollows in crystals derived from screw dislocation was predicted by Frank (1951). The radius of a hollow core can be estimated by the following equation:

$$\mathbf{r = \mu B^2/8\pi^2\gamma} \qquad \textbf{(eq.1)}$$

where **r** is the radius of the hollow core [m], **μ** is the shear modulus [Pa], **B** is the magnitude of Burgers vector [m], **γ** is the specific surface energy [J/m^2]. In order to form a hollow core in hematite, the Burgers vector must exceed a critical dimension that is based on the shear modulus, **μ** (91 GPa) (Bass 1995) and surface energy, **γ** (4.38 J/m^2 for hematite (0001) surface) (Bulgakov et al. 2002). This critical Burgers vector is also given by the energy minimization approach described by Frank (1951):

$$\mathbf{B > 66\ \pi\gamma/\mu} \qquad \textbf{(eq.2)}$$

where the right term, 66 πγ/μ, equals 9.98 nm for hematite. Hence the Burgers vector magnitude has to be greater than 9.98 nm in hematite in order to make a hollow core and the radius of the hollow core has to be larger than 26.21 nm, as estimated from eq.1. As shown in Figure 3a, the diameter of observed pore in a hematite nanoparticle is not greater than 3 nm, which is smaller than the calculated value (26.21 nm) by an order of magnitude. The lattice constants of hematite, a = 0.5038

nm and c = 1.3772 nm (Blake et al. 1966), are not large enough to generate Burgers vectors larger than 10 nm. Although Frank's theory contains some approximations such as isotropic elastic constants, the discrepancy between theoretical and experimental results suggests that the formation of nanopores and the crystal growth of this hematite are not just due to spiral growth from screw dislocations.

The morphology of nanopores within our hematite nanocrystals is also indicative of a formation mechanism unrelated to screw dislocations. If the nanopores were formed due to spiral growth from screw dislocations, one might expect straight, crystallographically-oriented linear pores such as those found in GaN thin films, in which mostly straight nanopipes are normal to the (0001) planes (Qian et al. 1995; Jacobs et al. 2008). In order to closely examine the morphology of nanopores within our hematite nanocrystals, we utilized tomography. In Figure 6, a tomographic reconstruction of hematite nanocrystals is shown. Nanopores are shaded in blue within the nanoparticulate hematite, which is shaded yellow (Movie 2 in the Data Repository also contains a 3D reconstruction of the nanocrystal and internal nanoporous structures). It is evident from the figure, as well as the movie (see Movie 2 the Data Repository available online), that the nanopores are not straight or oriented in any particular direction within the nanocrystals. It should also be noted that some of the nanopores are fully contained within the nanocrystals. If the nanopores were formed *via* a screw dislocation, it would be expected that the nanopores would contact the nanocrystal surfaces (Frank 1951; Si et al. 1997) which is not the case for our system.

As screw dislocations appear to be an unlikely cause of nanopores formation, we propose an alternative mechanism based upon volume differences between the precursor material and end product. Hematite nanocrystals in this study were transformed from ferrihydrite nanoparticles as described above (Fischer and Schwertmann 1975; Cornell et al. 1989). The chemical compositions of the precursor (ferrihydrite) and the final product (hematite) were recently reported as $Fe_{8.2}O_{8.5}(OH)_{7.4}\cdot 3H_2O$ and $Fe_2O_3\cdot 0.2H_2O$, respectively, based on crystal structure, chemical, and thermal analyses (Michel et al. 2007; Michel et al. 2010). These chemical compositions suggest that 1 mole of ferrihydrite transforms into 4.1 moles of hematite and 5.8 moles of H_2O, judging from the stoichiometry. The volume change in this transformation can be calculated as a 26.4 % reduction using the following values for formula weight and density: 721.4 g/mol and 4.3×10^6 g/m^3 for ferrihydrite and 159.7 g/mol and 5.3×10^6 g/m^3 for hematite, respectively (Michel et al. 2010). This simple calculation implies that crystallization of ferrihydrite into hematite causes a drastic reduction in the volume of the transforming solid phase and results, in part, in the generation of internal pores filled with H_2O such as nanopores in nanohematite in this study. It is also well known that the volume reduction associated with the dehydration of hydrated oxides can produce anhydrous porous material (Naono et al. 1987; Apblett et al. 2003; Yu et al. 2004), which is consistent with the proposed formation mechanism of nanopores in this study.

Time-resolved TEM observation on the transformation of ferrihydrite into hematite was carried out by Fischer and Schwertmann (1975). These authors reported that the first visible change was the

formation of denser aggregates 10 – 20 times as large as the initial ferrihydrite particles of which average diameter is about 5 nm. Their TEM observation also suggested that these aggregates gradually crystallize into hematite nanoparticles with rhombohedral shape with some imperfections such as fissures and holes. Recently, Yuwono et al. (2010) used cryo-TEM to describe the nanoporous structure of ferrihydrite aggregates (under the experimental conditions of their work, the ferrihydrite converts to goethite, α-FeOOH). On the basis of these previous studies (Fischer and Schwertmann 1975, Yuwono et al. 2010), we propose the formation mechanism of a single crystal of nano-sized rhombohedral hematite with nanopores in Figure 7. First, nanoparticles of a poorly crystallized precursor (ferrihydrite) are formed by the hydrolysis of ferric nitrate, and then the ferrihydrite precursors aggregate without aligning in any particular orientation. In aqueous media, the shape of the resulting aggregate should be three-dimensionally isotropic, most likely spherical or ellipsoidal, since particles can move freely. Subsequently, the phase transformation from poorly-crystalline ferrihydrite to crystalline hematite occurs, resulting in the formation of single crystals of hematite with rhombohedral morphology. During crystallization, the volume of the transforming aggregate shrinks as mentioned above and internal pores form along particle boundaries.

A notable feature of the nanoporous hematite crystals is their faceted rhombohedral morphology, which would suggest that during growth the system was close to equilibrium conditions (i.e., low supersaturation and low growth rate, Herring 1951; Williams and Bartelt 1989). Under such

equilibrium conditions, it might not be expected that high surface area structures such as nanopores would remain during growth in contrast to the above-mentioned observation. To make a well-defined crystal face from the aggregate of the poorly-crystalline precursor, it is necessary for Fe and O atoms to move and thus atomic diffusion on the crystal surface should be fast enough to achieve the equilibrium condition. On the other hand, atomic diffusion inside the crystal has to be relatively slow to preserve the grain boundaries as nanopores with a nanoparticulate precursor. Thus it is suggested that some chemical conditions, e.g., solution viscosity and diffusion coefficient, within an aggregate of precursors are likely to be much lower than those within the bulk surrounding medium due to the tightly confined space of grain boundaries as demonstrated by many previous studies (Hibara et al. 2002; Tsukahara et al. 2007; Kerisit and Liu 2009). In addition, Yin et al. (2004) demonstrated that nanoscale pores can develop inside cobalt oxide (CoO) nanocrystals through a mechanism analogous to void formation via the Kirkendall effect (Smigelskas and Kirkendall 1947), in which pores form because of the difference in diffusion rates between two components in a diffusion couple. The above-mentioned transformation of ferrihydrite into hematite, which is represented as $Fe_{8.2}O_{8.5}(OH)_{7.4}\cdot 3H_2O \rightarrow 4.1\ Fe_2O_3\cdot 0.2H_2O + 5.8\ H_2O$ (eq. 3), can also be considered as a phase separation process. This reaction formula and presence of nanopores in hematite nanocrystals suggest that H_2O produced by dehydration of ferrihydrite is segregated into the grain boundaries of precursors, remains there due to the tightly confined space of the grain boundaries, and results in the formation of nanopores inside the crystal. To make both hematite crystals and nanopores filled with

H_2O, both of the products in the right side of the reaction formula (eq. 3) have to move in opposite directions; in other words, they must separate from each other. Hence, the kinetic difference of atomic diffusion between inside and outside of the nanosized aggregate/crystal would account for the external crystal morphology and internal nanopore developments.

CONCLUSIONS

In summary, this paper reports the internal details of rhombohedral nanocrystals of hematite (α-Fe_2O_3), for the first time, in the form of nanoscale pores (nanopores) within crystals observed by HAADF-STEM tomography. Dissolution experiments of the hematite nanocrystals using ascorbic acid as a reductant demonstrated that these nanopores act as reactive sites for reductive dissolution. These results suggest that the large volume reduction concurrent with the formation of hematite nanocrystals from poorly crystalline ferrihydrite nanoparticle aggregates result in spaces at some of the former grain boundaries of the precursor nanoparticles. The spaces are the observed nanopores and this formation mechanism is different from those previously reported, such as hollow cores originating from screw dislocations (Frank 1951). These findings are of fundamental importance to understanding how certain crystal morphologies, internal structures, defects and reactive sites occur in nanocrystals formed from a poorly crystalline precursor.

Acknowledgement. Grants from the U.S. Department of Energy (DE-FG02-06ER15786) and

343 Virginia Tech's Nanoscale Characterization and Fabrication Laboratory provided financial support
344 for this study. T.E. acknowledges supports from the Japan Society for the Promotion of Science,
345 Research Fellowships for Young Scientists (PD20-1531), Japan Excellent Young Researcher
346 Overseas Visit Program, Grant-in-Aid for Research Activity Start-up (#23840049), and Fukada
347 Geological Institute (2011#7). D.M.A. acknowledges support from National Science Foundation
348 grant DEB-0610373 (Postdoctoral Fellowship) during part of this work. This manuscript was
349 completed during her current service at NSF. Any opinions, findings, and conclusions or
350 recommendations expressed in this material are those of the authors and do not necessarily reflect the
351 views of the National Science Foundation. We gratefully acknowledge the assistance of Dr.
352 Madeleine Schreiber (Virginia Tech) in providing the anaerobic chamber used for our experiments.
353 The authors are indebted to Dr. Martin Kunz, American Mineralogist Editor, and peer reviews from
354 Dr. Benjamin Gilbert and an anonymous source.

355

References cited

Apblett, A.W., Kuriyavar, S.I., and Kiran, B.P. (2003) Preparation of micron-sized spherical porous iron oxide particles. Journal of Materials Chemistry, 13, 983-985.

Banfield, J.F., Welch, S.A., Zhang, H., Ebert, T.T., and Penn, R.L. (2000) Aggregation-based crystal growth and microstructure development in natural iron oxyhydroxide biomineralization products. Science, 289, 751-754.

Banwart, S., Davies, S., and Stumm, W. (1989) The role of oxalate in accelerating the reductive dissolution of hematite (α-Fe_2O_3) by ascorbate. Colloids and Surfaces, 39, 303-309.

Bao, H., and Koch, P.L. (1999) Oxygen isotope fractionation in ferric oxide-water systems: low temperature synthesis. Geochimica et Cosmochimica Acta, 63, 599-613.

Bargar, J.R., Reitmeyer, R., and Davis, J.A. (1999) Spectroscopic confirmation of uranium (VI)—carbonato adsorption complexes on hematite. Environmental Science and Technology, 33, 2481-2484.

Bass, J.D. (1995) Elasticity of minerals, glasses, and melts. In T.J. Ahrens, Ed. Mineral physics and crystallography: A handbook of physical constants, 2, p. 45-63. American Geophysical Union, Washington, DC.

Blake, R.L., Hessevick, R.E., Zoltai, T., and Finger, L.W. (1966) Refinement of the hematite structure. American Mineralogist, 51, 123-129.

Boudeulle, M., and Muller, J.-P. (1988) Structural characteristics of hematite and goethite and their relationships with kaolinite in a laterite from Cameroon. A TEM study. Bulletin de Minéralogie, 111, 149-166.

Bulgakov, N.N., Sadykov, V.A., Lunin, V.V., and Kemnitz, E. (2002) Surface energies and heats of oxygen adsorption in ceria/ceria-zirconia solid solutions: Analysis by semiempirical interacting bonds method. Reaction Kinetics and Catalysis Letters, 76, 111-116.

Buxbaum, G. (1998) Industrial inorganic pigments, 3rd edition. 315 p. Wiley-VCH, Weinheim.

Carbone, C., Di Benedetto, F., Marescotti, P., Martinelli, A., Sangregorio, C., Cipriani, C., Lucchetti, G., and Romanelli, M. (2005) Genetic evolution of nanocrystalline Fe oxide and oxyhydroxide assemblages from the Libiola mine (eastern Liguria, Italy): structural and microstructural investigations. European Journal of Mineralogy, 17, 785-795.

Christensen, A.N., Convert, P., and Lehmann, M.S. (1980) Hydrothermal crystal-growth rate of goethite and hematite from amorphous iron (III) hydroxide investigated by X-ray-diffraction and neutron-diffraction. Acta Chemica Scandinavica Series A: Physical and Inorganic Chemistry, 34, 771-776.

Christensen, P.R., Morris, R.V., Lane, M.D., Bandfield, J.L., and Malin, M.C. (2001) Global mapping of Martian hematite mineral deposits: Remnants of water-driven processes on early Mars. Journal of Geophysical Research, 106, 23873-23885.

Cook, J.M., O'Keefe, M.A., Smith, D.J., and Stobbs, W.M. (1983) The high resolution electron

393 microscopy of stacking defects in Cu-Zn-Al shape memory alloy. Journal of Microscopy, 129,
394 295-306.
395 Cornell, R.M., Giovanoli, R., and Schneider, W. (1989) Review of the hydrolysis of iron (III) and the
396 crystallization of amorphous iron (III) hydroxide hydrate. Journal of Chemical Technology &
397 Biotechnology, 46, 115-134.
398 Cornell, R.M., and Schwertmann, U. (2003) The iron oxides: Structure, properties, reactions,
399 occurrences, and uses. 703 p. Wiley-VCH Verlag Gmbh & Co., Weinheim.
400 Cowley, J.M., and Moodie, A.F. (1957) The scattering of electrons by atoms and crystals. I. A new
401 theoretical approach. Acta Crystallographica, 10, 609-619.
402 Dos Santos Afonso, M., Morando, P.J., Blesa, M.A., Banwart, S., and Stumm, W. (1990) The
403 reductive dissolution of iron oxides by ascorbate: The role of carboxylate anions in
404 accelerating reductive dissolution. Journal of Colloid and Interface Science, 138, 74-82.
405 Echigo, T., Aruguete, D.M., Murayama, M., and Hochella, M.F. (2012) Influence of size,
406 morphology, surface structure, and aggregation state on reductive dissolution of hematite
407 nanoparticles with ascorbic acid. Geochimica et Cosmochimica Acta, 90, 149-162.
408 Eggleston, C.M., Shankle, A.J.A., Moyer, A.J., Cesar, I., and Gr tzel, M. (2009) Anisotropic
409 photocatalytic properties of hematite. Aquatic Sciences, 71, 151-159.
410 Fischer, W.R., and Schwertmann, U. (1975) Formation of hematite from amorphous iron(III)
411 hydroxide. Clays and Clay Minerals, 23, 33-37.
412 Frank, F.C. (1951) Capillary equilibria of dislocated crystals. Acta Crystallographica, 4, 497-501.
413 Friedrich, H.; McCartney, M.R.; Buseck, P.R. (2005) Comparison of intensity distributions in
414 tomograms from BF TEM, ADF STEM, HAADF STEM, and calculated tilt series
415 Ultramicroscopy, 106, 18-27.
416 Fujita, T., Qian, L.H., Inoke, K., Erlebacher, J., and Chen, M.W. (2008) Three-dimensional
417 morphology of nanoporous gold. Applied Physics Letters, 92, 251902-251902-3.
418 Heijna, M.C.R., van den Dungen, P.B.P., van Enckevort, W.J.P., and Vlieg, E. (2006) An atomic force
419 microscopy study of the (001) surface of triclinic hen egg-white lysozyme crystals. Crystal
420 Growth & Design, 6, 1206-1213.
421 Herring, C. (1951) Some theorems on the free energies of crystal surfaces. Physical Review, 82,
422 87-93.
423 Hibara, A., Saito, T., Kim, H.B., Tokeshi, M., Ooi, T., Nakao, M., and Kitamori, T. (2002)
424 Nanochannels on a fused-silica microchip and liquid properties investigation by
425 time-resolved fluorescence measurements. Analytical Chemistry, 74, 6170-6176.
426 Hochella, M.F., Lower, S.K., Maurice, P.A., Penn, R.L., Sahai, N., Sparks, D.L., and Twining, B.S.
427 (2008) Nanominerals, mineral nanoparticles, and Earth systems. Science, 319, 1631-1635.
428 Hochella, M.F., Kasama, T., Putnis, A., Putnis, C.V., and Moore, J.N. (2005) Environmentally
429 important, poorly crystalline Fe/Mn hydrous oxides: Ferrihydrite and a possibly new
430 vernadite-like mineral from the Clark Fork River Superfund Complex. American

Mineralogist, 90, 718-724.

Hochella, M.F., Moore, J.N., Golla, U., and Putnis, A. (1999) A TEM study of samples from acid mine drainage systems: metal-mineral association with implications for transport. Geochimica et Cosmochimica Acta, 63, 3395-3406.

Jacobs, B.W., Crimp, M.A., McElroy, K., and Ayres, V.M. (2008) Nanopipes in Gallium Nitride Nanowires and Rods. Nano Letters, 8, 4353-4358.

Jambor, J.L., and Dutrizac, J.E. (1998) Occurrence and constitution of natural and synthetic ferrihydrite, a widespread iron oxyhydroxide. Chemical Reviews, 98, 2549-2586.

Janney, D.E., and Banfield, J.F. (1998) Distribution of cations and vacancies and the structure of defects in oxidized intermediate olivine by atomic-resolution TEM and image simulation. American Mineralogist, 83, 799-810.

Johnston, J.H., and Lewis, D.G. (1983) A detailed study of the transformation of ferrihydrite to hematite in an aqueous medium at 92 °C. Geochimica et Cosmochimica Acta, 47, 1823-1831.

Kerisit, S., and Liu, C. (2009) Molecular simulations of water and ion diffusion in nanosized mineral fractures. Environmental Science and Technology, 43, 777-782.

Klein, M., P., Jacobs, B., W., Ong, M., D., Fares, S., J., Robinson, D., B., Stavila, V., Wagner, G.J., and Arslan, I. (2011) Three-dimensional pore evolution of nanoporous metal particles for energy storage. Journal of the American Chemical Society, 133, 9144-9147.

Kletetschka, G., Wasilewski, P.J., and Taylor, P.T. (2000) Hematite vs. magnetite as the signature for planetary magnetic anomalies? Physics of the Earth and Planetary Interiors, 119, 259-267.

Kogure, T., and Inoue, A. (2005) Determination of defect structures in kaolin minerals by high-resolution transmission electron microscopy (HRTEM). American Mineralogist, 90, 85-89.

Kormann, C., Bahnemann, D.W., and Hoffmann, M.R. (1989) Environmental photochemistry: Is iron oxide (hematite) an active photocatalyst? A comparative study: α-Fe_2O_3, ZnO, TiO_2. Journal of Photochemistry and Photobiology A: Chemistry, 48, 161-169.

Land, T.A., Malkin, A.J., Kuznetsov, Y.G., McPherson, A., and De Yoreo, J.J. (1995) Mechanisms of protein crystal growth: An atomic force microscopy study of canavalin crystallization. Physical review letters, 75, 2774-2777.

Matijević, E., and Scheiner, P. (1978) Ferric hydrous oxide sols: III. Preparation of uniform particles by hydrolysis of Fe (III)-chloride,-nitrate, and-perchlorate solutions. Journal of Colloid and Interface Science, 63, 509-524.

Michel, F.M., Barrón, V., Torrent, J., Morales, M.P., Serna, C.J., Boily, J.F., Liu, Q., Ambrosini, A., Cismasu, A.C., and Brown, G.E. (2010) Ordered ferrimagnetic form of ferrihydrite reveals links among structure, composition, and magnetism. Proceedings of the National Academy of Sciences, 107, 2787-2792.

Michel, F.M., Ehm, L., Antao, S.M., Lee, P.L., Chupas, P.J., Liu, G., Strongin, D.R., Schoonen, M.A.A., Phillips, B.L., and Parise, J.B. (2007) The structure of ferrihydrite, a nanocrystalline

material. Science, 316, 1726-1729.

Myerson, A.S. (2002) Handbook of industrial crystallization, 2nd edition. 304 p. Butterworth-Heinemann, Boston.

Naono, H., Nakai, K., Sueyoshi, T., and Yagi, H. (1987) Porous texture in hematite derived from goethite: Mechanism of thermal decomposition of geothite. Journal of Colloid and Interface Science, 120, 439-450.

Navrotsky, A., Ma, C., Lilova, K., and Birkner, N. (2010) Nanophase transition metal oxides show large thermodynamically driven shifts in oxidation-reduction equilibria. Science, 330, 199-201.

Navrotsky, A., Mazeina, L., and Majzlan, J. (2008) Size-driven structural and thermodynamic complexity in iron oxides. Science, 319, 1635-1638.

Park, G.S., Shindo, D., Waseda, Y., and Sugimoto, T. (1996) Internal structure analysis of monodispersed pseudocubic hematite particles by electron microscopy. Journal of Colloid and Interface Science, 177, 198-207.

Peng, D., Beysen, S., Li, Q., Sun, Y., and Yang, L. (2010) Hydrothermal synthesis of monodisperse α-Fe_2O_3 hexagonal platelets. Particuology, 8, 386-389.

Qian, W., Skowronski, M., Doverspike, K., Rowland, L.B., and Gaskill, D.K. (1995) Observation of nanopipes in α-GaN crystals. Journal of Crystal Growth, 151, 396-400.

Rösner, H., Parida, S., Kramer, D., Volkert, C.A., and Weissmüler, J. (2007) Reconstructing a nanoporous metal in three dimensions: an electron tomography study of dealloyed gold leaf. Advanced Engineering Materials, 9, 535-541.

Redman, A.D., Macalady, D.L., and Ahmann, D. (2002) Natural organic matter affects arsenic speciation and sorption onto hematite. Environmental Science and Technology, 36, 2889-2896.

Reimer, L., and Kohl, H. (2008) Transmission electron microscopy: Physics of image formation. 590 p. Springer Verlag, New York.

Rodriguez, R.D., Demaille, D., Lacaze, E., Jupille, J., Chaneac, C., and Jolivet, J.P. (2007) Rhombohedral shape of hematite nanocrystals synthesized via thermolysis of an additive-free ferric chloride solution. Journal of Physical Chemistry C, 111, 16866-16870.

Schwertmann, U., Friedl, J., Stanjek, H., Murad, E., and Bender Koch, C. (1998) Iron oxides and smectites in sediments from the Atlantis II Deep, Red Sea. European Journal of Mineralogy, 10, 953-967.

Schwertmann, U., and Murad, E. (1983) Effect of pH on the formation of goethite and hematite from ferrihydrite. Clays and Clay Minerals, 31, 277-284.

Shi, L., Xu, Y.M., Li, Q., Wu, Z.Y., Chen, F.R., and Kai, J.J. (2007) Single crystalline ZnS nanotubes and their structural degradation under electron beam irradiation. Applied Physics Letters, 90, 211910.

Shindo, D., Lee, B.T., Waseda, Y., Muramatsu, A., and Sugimoto, T. (1993) Crystallography of

platelet-type hematite particles by electron microscopy. Materials Transactions JIM, 34, 580-585.

Si, W., Dudley, M., Glass, R., Tsvetkov, V., and Carter, C. (1997) Hollow-core screw dislocations in 6H-SiC single crystals: A test of Frank's theory. Journal of Electronic Materials, 26, 128-133.

Smigelskas, A.D., and Kirkendall, E.O. (1947) Zinc diffusion in alpha brass. Transactions of the American Institute of Mining and Metallurgical Engineers, 171, 130-142.

Storm, A.J., Chen, J.H., Ling, X.S., Zandbergen, H.W., and Dekker, C. (2005) Electron-beam-induced deformations of SiO_2 nanostructures. Journal of Applied Physics, 98, 014307.

Sugimoto, T., Wang, Y., Itoh, H., and Muramatsu, A. (1998) Systematic control of size, shape and internal structure of monodisperse α-Fe_2O_3 particles. Colloids and Surfaces A: Physicochemical and Engineering Aspects, 134, 265-279.

Sunagawa, I. (2005) Crystals: growth, morphology, and perfection. 295 p. Cambridge University Press, Cambridge, UK.

Suter, D., Banwart, S., and Stumm, W. (1991) Dissolution of hydrous iron (III) oxides by reductive mechanisms. Langmuir, 7, 809-813.

Tsukahara, T., Hibara, A., Ikeda, Y., and Kitamori, T. (2007) NMR study of water molecules confined in extended nanospaces. Angewandte Chemie International Edition, 46, 1180-1183.

Tsukimura, K., Suzuki, M., Suzuki, Y., and Murakami, T. (2010) Kinetic theory of crystallization of nanoparticles. Crystal Growth & Design, 10, 3596-3607.

Utsunomiya, S., and Ewing, R.C. (2003) Application of high-angle annular dark field scanning transmission electron microscopy, scanning transmission electron microscopy-energy dispersive X-ray spectrometry, and energy-filtered transmission electron microscopy to the characterization of nanoparticles in the environment. Environmental Science and Technology, 37, 786-791.

Vu, H.P., Shaw, S., and Benning, L.G. (2008) Transformation of ferrihydrite to hematite: an in situ investigation on the kinetics and mechanisms. Mineralogical Magazine, 72, 217.

Waychunas, G.A., Kim, C.S., and Banfield, J.F. (2005) Nanoparticulate iron oxide minerals in soils and sediments: unique properties and contaminant scavenging mechanisms. Journal of Nanoparticle Research, 7, 409-433.

Wigginton, N.S., Haus, K.L., and Hochella, M.F. (2007) Aquatic environmental nanoparticles. Journal of Environemtal Monitoring, 9, 1306-1316.

Williams, E.D., and Bartelt, N.C. (1989) Surface faceting and the equilibrium crystal shape. Ultramicroscopy, 31, 36-48.

Wu, C., Yin, P., Zhu, X., OuYang, C., and Xie, Y. (2006) Synthesis of hematite (α-Fe_2O_3) nanorods: Diameter-size and shape effects on their applications in magnetism, lithium ion battery, and gas sensors. J. Phys. Chem. B, 110, 17806-17812.

Yanina, S.V., and Rosso, K.M. (2008) Linked reactivity at mineral-water interfaces through bulk

crystal conduction. Science, 320, 218-222.

Yin, Y., Rioux, R.M., Erdonmez, C.K., Hughes, S., Somorjai, G.A., and Alivisatos, A.P. (2004) Formation of hollow nanocrystals through the nanoscale Kirkendall effect. Science, 304, 711-714.

Yu, J.C., Xu, A., Zhang, L., Song, R., and Wu, L. (2004) Synthesis and characterization of porous magnesium hydroxide and oxide nanoplates. The Journal of Physical Chemistry B, 108, 64-70.

552 **Figure captions**

553 **Figure 1.** TEM image of hematite nanocrystals showing rhombohedral shape. Arrows indicate
554 crystal imperfections which are barely observable.

555 **Figure 2.** (a) HRTEM image of hematite nanocrystal showing a hollow core (nanopore)
556 perpendicular to the page. (b) HAADF-STEM image of hematite nanocrystal showing
557 nanopores running through the crystals. (c) Isosurface image of hematite nanocrystal
558 shown in (b). Nanoscale dimple on the surface of crystal was found by HAADF-STEM
559 tomography. A 3D movie of this tomographic reconstruction is available online (see
560 Movie 1 in the Data Repository). (d) Two slices perpendicular to each other taken from
561 the tomography image shown in (c). Nanopores run inside the crystal.

562 **Figure 3.** Hematite nanocrystals showing a rhombohedral morphology with nanopores clearly
563 visible. (a) HAADF-STEM image taken at 200kV with a field emission source. Black
564 and white arrows mark edges with high and low contrast, respectively, keeping in mind
565 the sensitivity of HAADF-STEM image contrast to the average atomic number along
566 the electron beam path and the path length through the material depending on the shape
567 and orientation of the particle, and voids within the particle. (b) HRTEM image taken at
568 200kV with a field emission source.

569 **Figure 4.** TEM images taken (a) immediately after inserting the sample and (b) after about 15
570 minutes. White and black arrows show a nanopore within a hematite nanocrystal and
571 irregular surface morphology of another hematite nanocrystal, respectively.

572 **Figure 5.** HRTEM images of hematite nanocrystals. Arrowheads mark nanopores that reach the
573 surface of crystals. (a) Hematite before dissolution showing nanopores. (b) Hematite
574 after dissolution showing dramatically enlarged funnel-shaped openings of pre-existing
575 nanopores.

576 **Figure 6.** Isosurface image of hematite nanocrystals. The internal nanopores are light green in
577 color. The inset shows the orientation of the nanopores within the hematite crystals. A
578 3D movie of this tomographic reconstruction is available online (see Movie 2 in the
579 Data Repository).

580 **Figure 7.** Schematic illustration of crystallization routes of hematite from ferrihydrite
581 nanoparticles. In this model, aggregation of rounded Ft particles occurs first, resulting
582 in the formation of a spherical or ellipsoidal aggregate. Subsequently Ft crystallizes into
583 Ht with a concurrent reduction in volume indicated by white arrows (-26.4 %). The
584 resulting morphology of the nanocrystal is rhombohedral, with nanopores formed at the
585 grain boundaries of the precursors due to the volume reduction with crystallization.

586

587 **Captions for Deposit Items**

588 **Movie 1.** Isosurface representation of hematite nanocrystals showing a nanoscale pore on one of
589 the nanohematite surfaces.

590 **Movie 2.** Isosurface representation of hematite nanocrystals showing the internal nanopores.

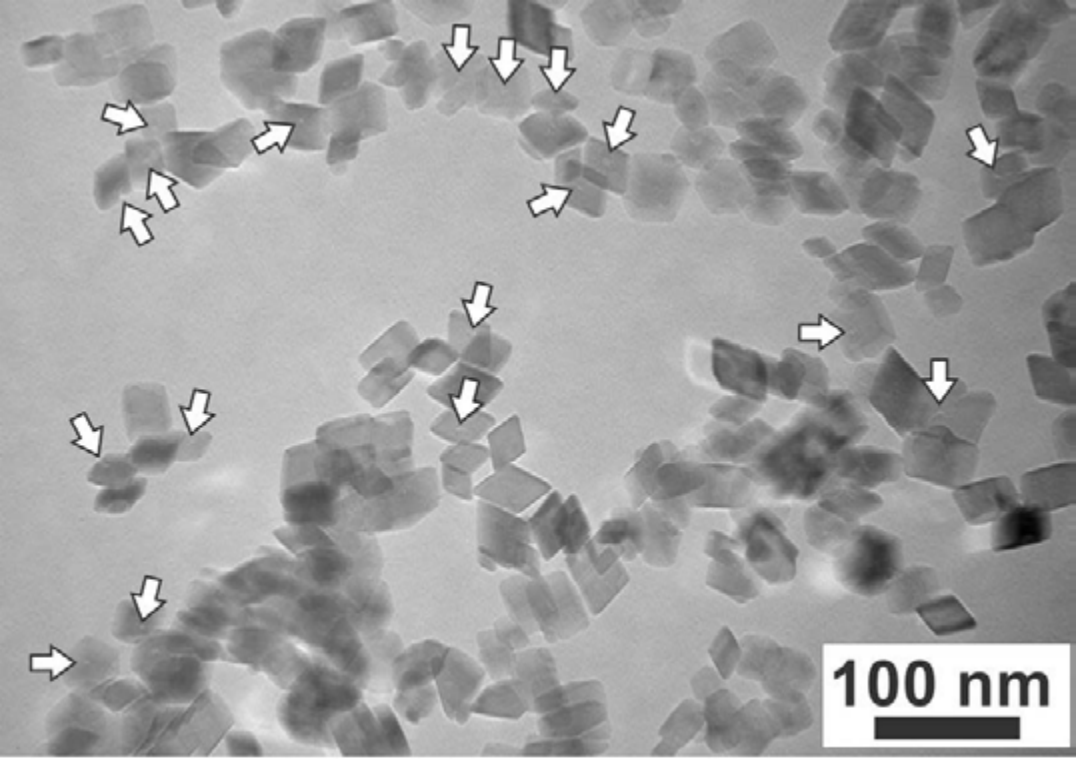

Fig. 1 (Echigo et al.)

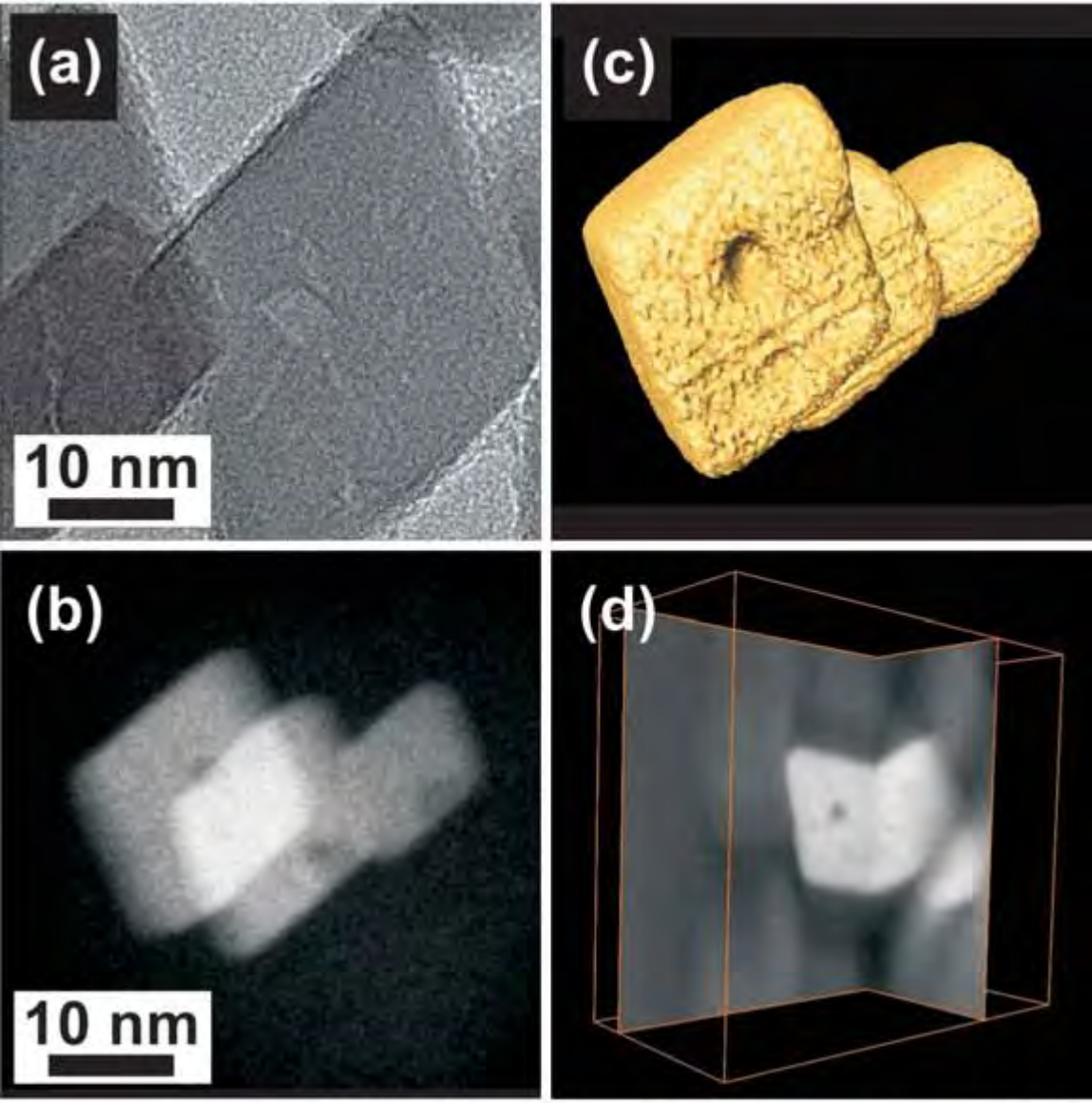

Fig. 2 (Echigo et al.)

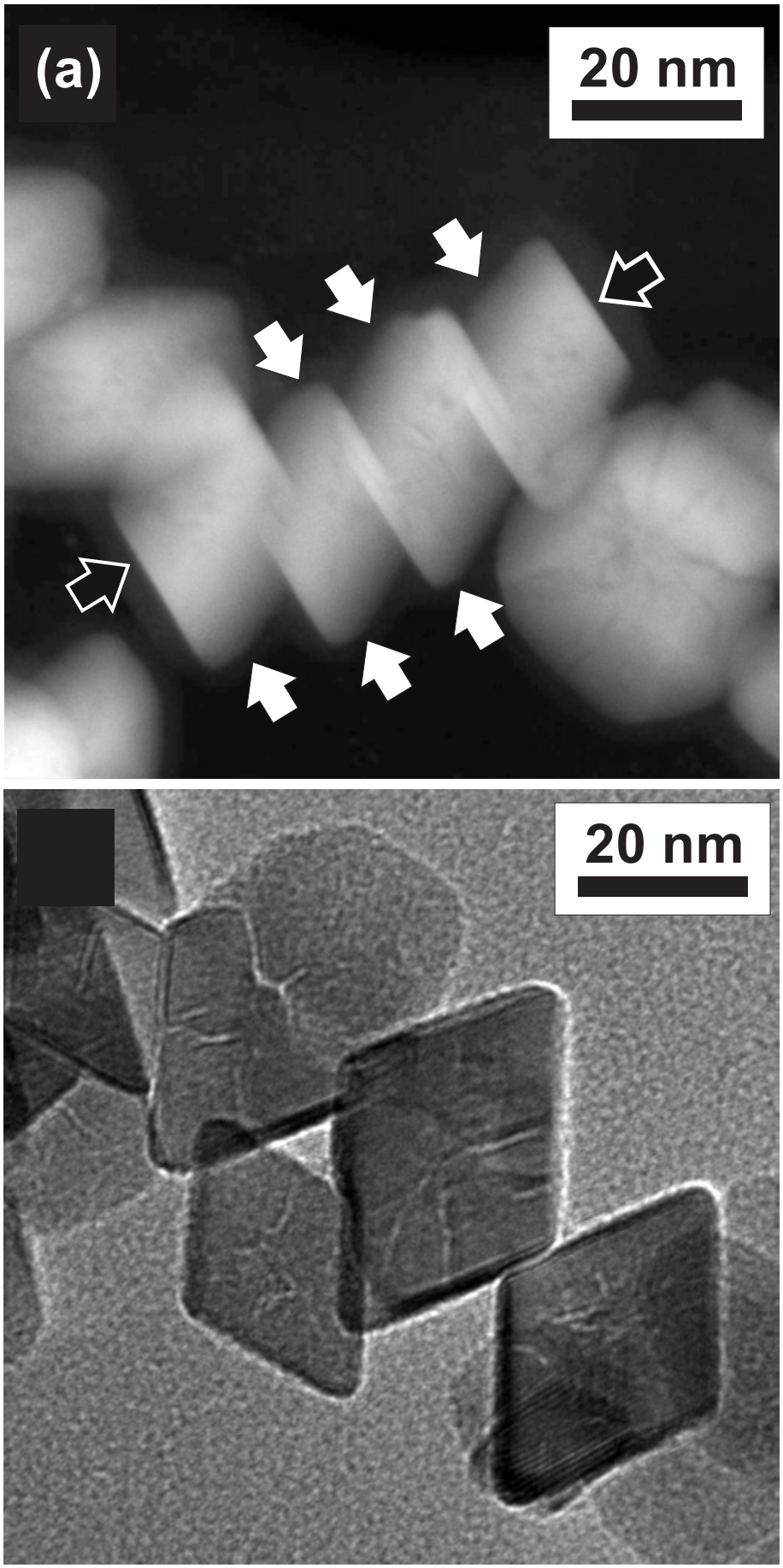
(a)
20 nm
20 nm

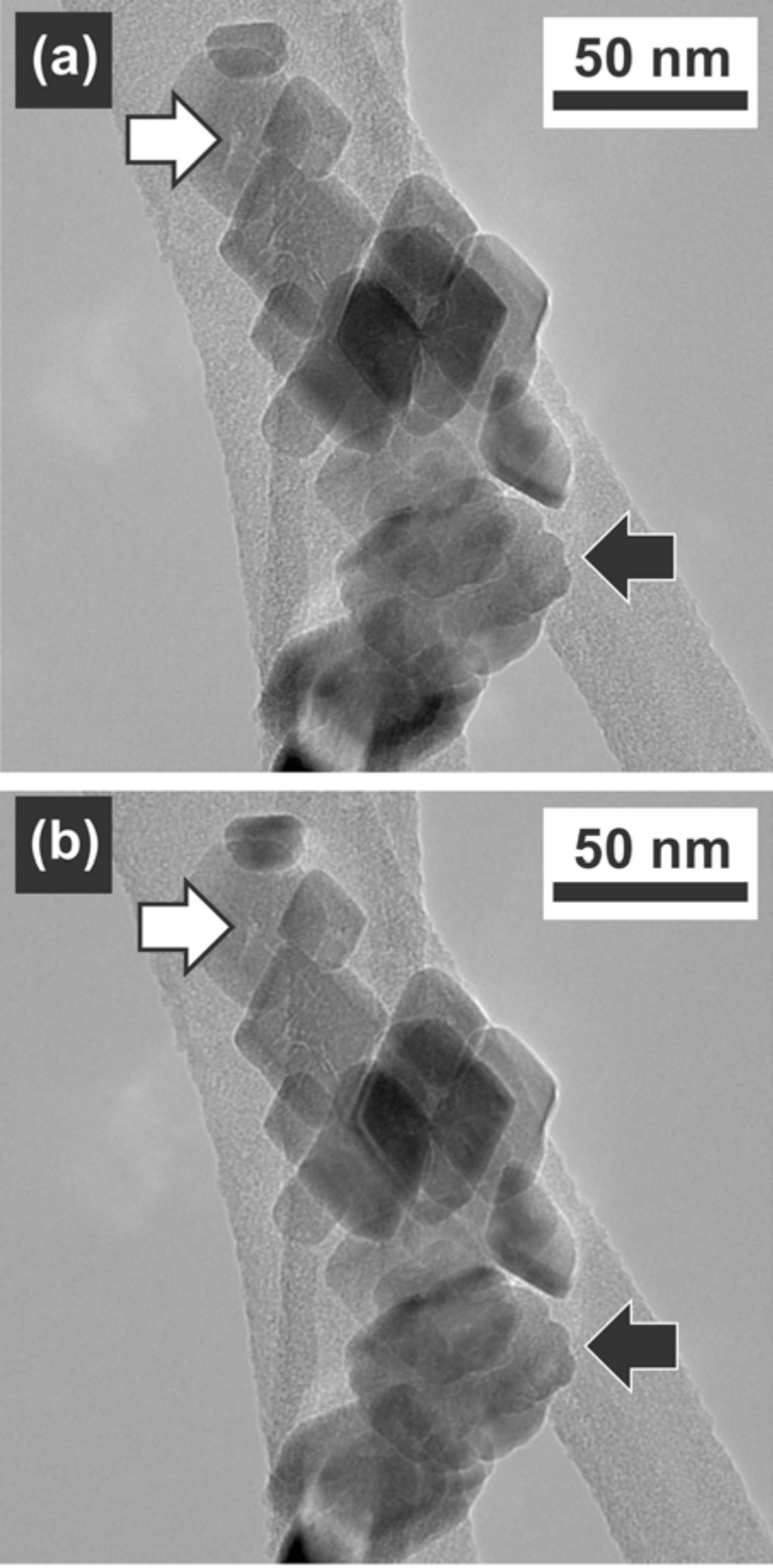

Fig. 4 (Echigo et al.)

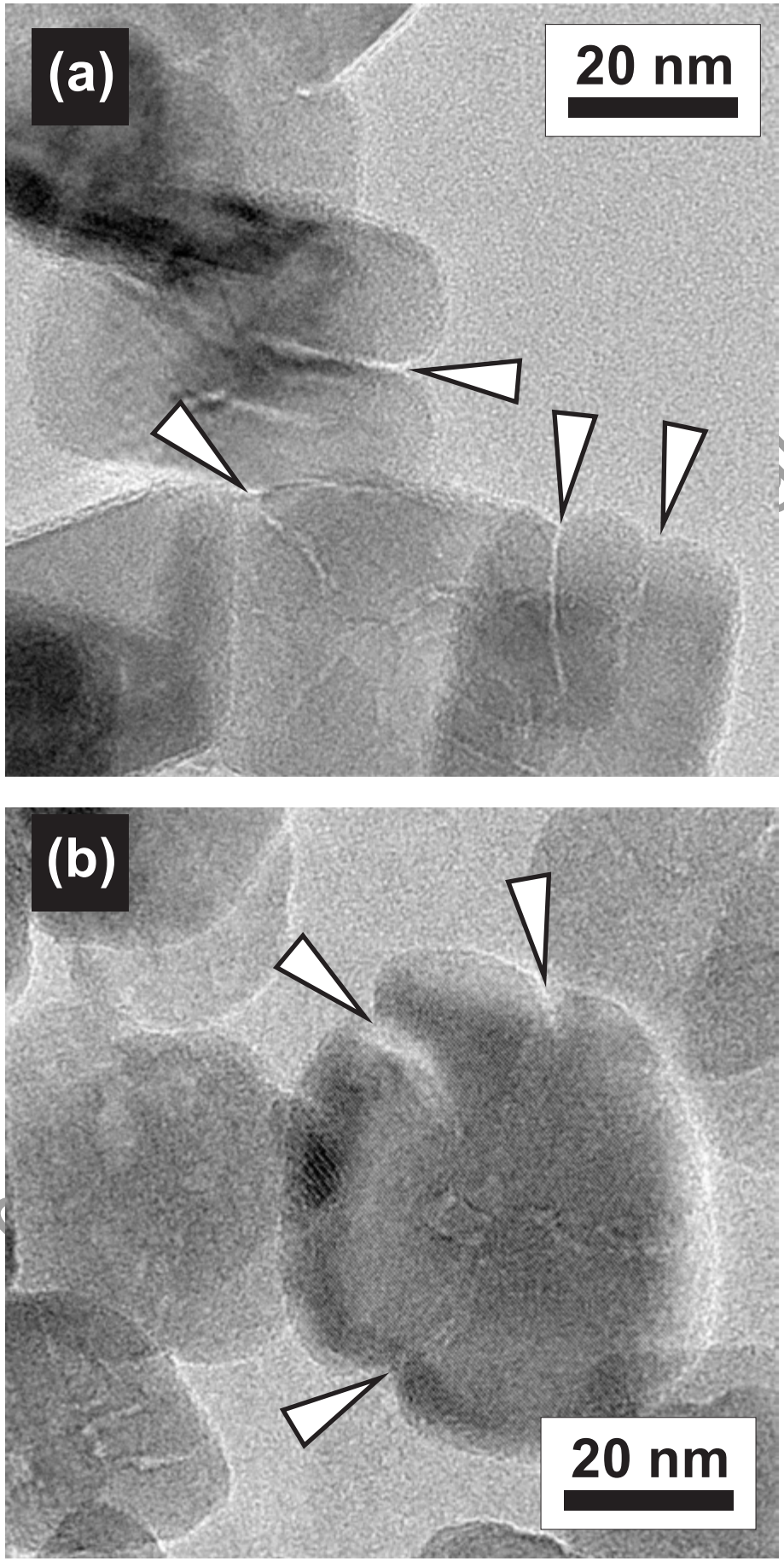

Fig. 5 (Echigo et al.)

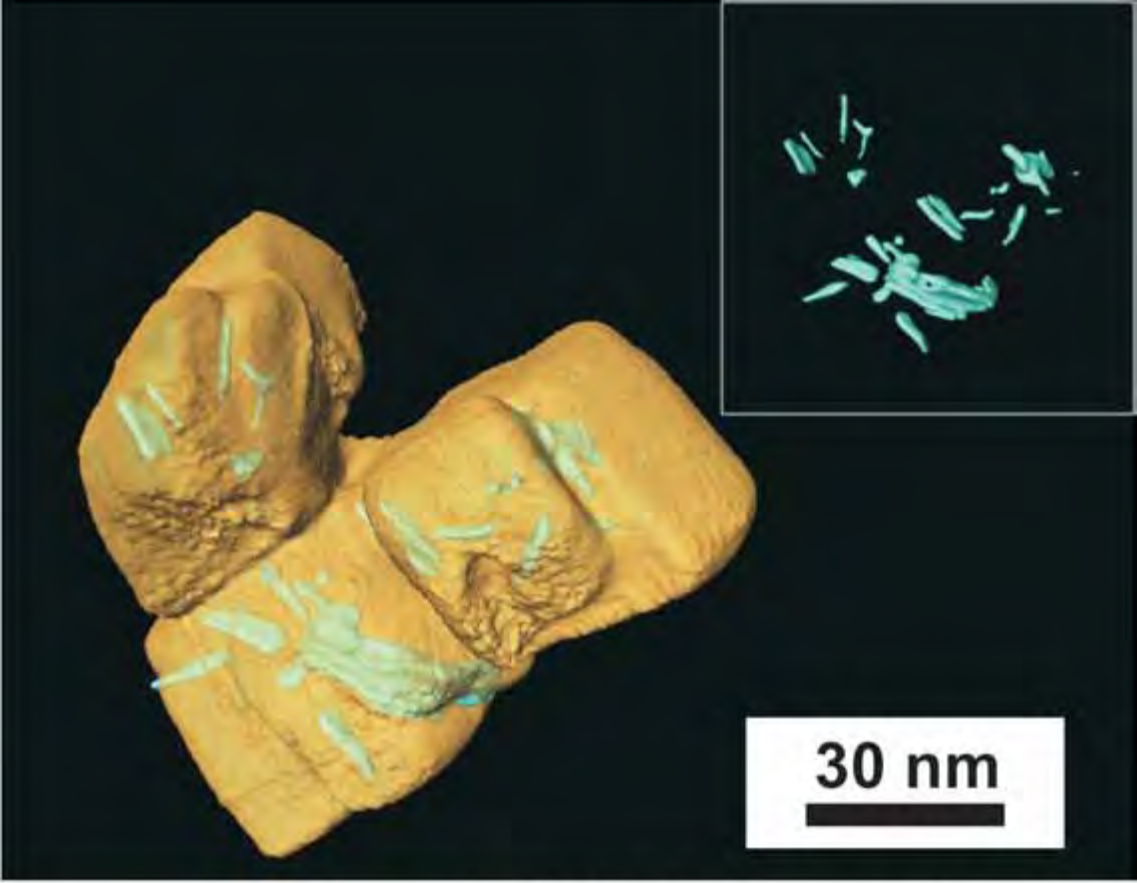

Fig. 6 (Echigo et al.)

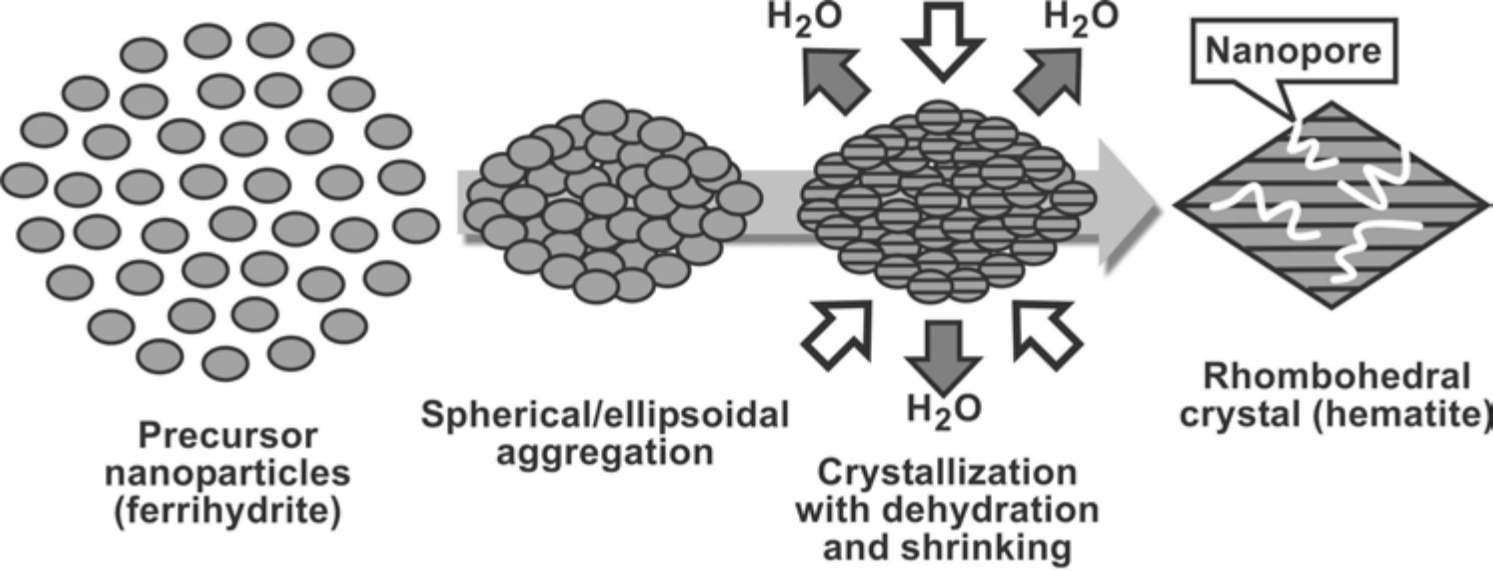

Fig. 7 (Echigo et al.)